Unraveling the electrolyte properties of Na_3SbS_4 through computation and experiment

Larry E. Rush, Jr.,[1] Zachary D. Hood,[2] and N. A. W. Holzwarth[1,*]

[1]*Department of Physics, Wake Forest University, Winston-Salem, North Carolina 27109-7507, USA*

[2]*School of Chemistry and Biochemistry, Georgia Institute of Technology, Atlanta, Georgia 30332, USA and Center for Nanophase Materials Sciences, Oak Ridge National Laboratory, Oak Ridge, Tennessee 37831, USA*

(Received 12 September 2017; published 11 December 2017)

Solid-state sodium electrolytes are expected to improve next-generation batteries on the basis of favorable energy density and reduced cost. Na_3SbS_4 represents a new solid-state ion conductor with high ionic conductivities in the mS/cm range. Here, we explore the tetragonal phase of Na_3SbS_4 and its interface with metallic sodium anode using a combination of experiments and first-principles calculations. The computed Na-ion vacancy migration energies of 0.1 eV are smaller than the value inferred from experiment, suggesting that grain boundaries or other factors dominate the experimental systems. Analysis of symmetric cells of the electrolyte—Na/Na_3SbS_4/Na—show that a conductive solid electrolyte interphase forms. Computer simulations infer that the interface is likely to be related to Na_3SbS_3, involving the conversion of the tetrahedral SbS_4^{3-} ions of the bulk electrolyte into trigonal pyramidal SbS_3^{3-} ions at the interface.

DOI: 10.1103/PhysRevMaterials.1.075405

I. INTRODUCTION

Recent efforts to improve energy storage technology has driven renewed interest in the detailed study of electrolyte materials in terms of their ion conduction mechanisms and in terms of their interfaces with electrodes. In the present combined experimental and computational study, we focus on an exemplary system, Na_3SbS_4, which is a promising electrolyte for all solid-state Na-ion batteries, recently identified by three independent groups [1–4].

Na_3SbS_4 comes from a family of structurally and chemically related materials based on Na_3PS_4 reported by Hayashi *et al.* [5]. The family, which includes Na_3PS_4, Na_3PSe_4, Na_3SbS_4, and Na_3SbSe_4, has been the focus of several studies [1–11]. While the family of materials is characterized by tetragonal-to-cubic phase transitions, the authors conclude that high ionic conductivity is attributed to Na-ion vacancy hopping between nearest-neighbor sites along the crystallographic axes. Apparently, the geometry of low barrier ionic hopping found in these materials is consistent with the "design principle" found in other superionic conducting materials where ion diffusion was found to be superior in anion sublattices having bcc-like frameworks [12]. Within this family of materials, Na_3SbS_4 stands out in terms of its high ionic conductivity of 1–3 mS/cm at 25 °C, favorable synthesis, chemical stability in air, and compatibility with a Na metal anode [1–4].

In the present paper, we extend the experimental investigation reported in Ref. [1] and use first-principles computer modeling methods to examine details of the tetragonal phase of Na_3SbS_4. The focus of this study is on determining mechanisms of Na-ion migration and on developing models of interfaces with Na metal. We also examine the related material Na_3SbS_3 which has been shown to exhibit ionic conductivity [13], and which may form at the Na_3SbS_4/Na interface.

II. METHODS

A. Experimental methods

1. Synthesis of tetragonal Na_3SbS_4

The synthesis of Na_3SbS_4 was based on previous work at Oak Ridge National Laboratory [1]. In short, 4 g of $Na_3SbS_4 \cdot 9H_2O$ (Schlippe's salt from Pfaltz & Bauer) was ball milled with Y-ZrO_2 balls (3 and 5 mm) for 5 min using an 8000M SPEX Mixer/Mill. The powder was then sifted and transferred to a drying vessel, evacuated on a Schlenk line, and heated under vacuum to 150 °C for 1 h using a ramp rate of 5 °C/min. The final powder was transferred to an argon-filled glovebox for further processing.

2. Structural and compositional characterization

Identification of the crystalline phase for Na_3SbS_4 was conducted on a PANalytical X'pert Pro powder diffractometer with Cu $K\alpha$ radiation ($\lambda = 1.540\,56$ Å). All samples were prepared in a glovebox and the quartz slides were sealed with Kapton® films. Scanning electron microscopy (SEM) images were collected on a field-emission scanning electron microscope (Zeiss Merlin) at an acceleration voltage of 10.0 kV equipped with a custom-designed stage for handling air-sensitive materials such as metallic sodium [14]. Energy-dispersive x-ray spectroscopy (EDS) elemental mappings were completed with a Bruker EDS system at an acceleration voltage of 15.0 kV.

3. Electrochemical characterization

All samples were prepared for electrochemical measurements in an argon-filled glovebox. Tetragonal Na_3SbS_4 was cold-pressed at 300 MPa in an airtight cell designed by our group with Al/C blocking electrodes for all electrochemical impedance spectroscopy (EIS) measurements (Bio-Logic, VSP). EIS measurements were measured between 1 mHz and 1 MHz with an amplitude of 100.0 mV in a temperature-controlled chamber. For Arrhenius measurements, the temperature control chamber was ramped from 10 to 110 °C and allowed to equilibrate for 2 h before EIS measurements were

*natalie@wfu.edu

collected. The activation energy (E_a) was calculated from the formula

$$\sigma = \frac{C}{T} e^{-E_a/kT}, \tag{1}$$

where C denotes a temperature-independent constant, k represents the Boltzmann constant, T represents the temperature (in Kelvin) and E_a denotes the activation energy. This formula, which is presented in several textbooks and review articles [15–17], is based on near-equilibrium transport theory which relates the conductivity to the diffusion coefficient using the Nernst-Einstein relationship and the assumption of an Arrhenius temperature dependence of the the diffusion constant. The simple exponential form of $\sigma = \sigma_0 e^{-E_a'/kT}$ is also seen in the literature. However, since the simple exponential form is slightly less well-motivated by basic principles, we choose to use Eq. (1) instead.

Symmetric Na/Na_3SbS_4/Na cells were constructed by cold-pressing tetragonal Na_3SbS_4 at 300 MPa and carefully affixing two polished metallic sodium foils (Sigma Aldrich) to each side of the pellet in a Swagelok® cell. The symmetric cells were cycled at a current density of 0.1 mA/cm^2 for 40 cycles (30 min for each polarity). The interface between metallic sodium and tetragonal Na_3SbS_4 was analyzed with SEM/EDS analysis after fracturing the solid electrolyte pellets.

B. Computational methods

The computational methods used in this work are based on density functional theory [18,19], implemented by the projected augmented wave (PAW) [20] formalism. The PAW basis and projector functions were generated by the ATOMPAW [21] code and used in the QUANTUM ESPRESSO [22] package. Visualizations of the crystal structures were constructed using the XCRYSDEN [23,24] and VESTA [25] software packages.

The exchange-correlation function is approximated using the local-density approximation (LDA) [26]. The choice of LDA functional was made based on previous investigations [27–32] of similar materials which showed that the simulations are in good agreement with experiment, especially the fractional lattice parameters, the vibrational frequencies, and heats of formation. The simulated magnitudes of the lattice parameters, when systematically scaled by a factor of 1.02, are also in good agreement with experiment.

The partial densities of states were calculated from the expression

$$N^a(E) = \sum_{n\mathbf{k}} W_{\mathbf{k}} Q^a_{n\mathbf{k}} \delta(E - E_{n\mathbf{k}}), \tag{2}$$

as described in previous work [31,33]. Here a denotes an atomic site, $W_{\mathbf{k}}$ denotes the Brillouin zone sampling weight factor for wave vector $\mathbf{k}$, and $E_{n\mathbf{k}}$ denotes the band energy for band index n and wave vector $\mathbf{k}$. In practice, the δ function is represented by a Gaussian smoothing function with a width of 0.14 eV. For each eigenstate $n\mathbf{k}$ and atomic site a, the local density of states factor $Q^a_{n\mathbf{k}}$ is given by the charge within the augmentation sphere of radius r^a_c which can be well approximated by

$$Q^a_{n\mathbf{k}} \approx \sum_{ij} \langle \widetilde{\Psi}_{n\mathbf{k}} | p^a_{n_i l_i m_i} \rangle \langle p^a_{n_j l_j m_i} | \widetilde{\Psi}_{n\mathbf{k}} \rangle q^a_{n_i l_i; n_j l_i} \delta_{l_i l_j}, \tag{3}$$

in terms of the radial integrals

$$q^a_{n_i l_i; n_j l_i} \equiv \int_0^{r^a_c} dr\, \varphi^a_{n_i l_i}(r) \varphi^a_{n_j l_j}(r). \tag{4}$$

In these expressions, $|\widetilde{\Psi}_{n\mathbf{k}}\rangle$ represents a pseudowave function, $|p^a_{n_i l_i m_i}\rangle$ represents a PAW atomic projector function localized within the augmentation sphere about atomic site a and characterized with radial and spherical harmonic indices $n_i l_i m_i$ [20,21,34]. The function $\varphi^a_{n_i l_i}(r)$ represents the corresponding all-electron radial basis function. The augmentation radii used in this work are $r_c^{\mathrm{Na}} = 1.7$, $r_c^{\mathrm{Sb}} = 2.4$, and $r_c^{\mathrm{S}} = 1.7$ in bohr units. The reported partial densities of states, $\langle N^a(E) \rangle$, are averaged over sites of each type a.

The calculations were well converged with plane-wave expansions of the wave function including $|\mathbf{k} + \mathbf{G}|^2 \leqslant 64$ bohr^{-2}. The Brillouin zone integrals were evaluated by using uniform sampling volumes of 0.001 Å^{-3} or smaller.

Simulations of Na-ion migration were performed at constant volume in supercells constructed from the optimized conventional cells. In modeling charged defects of Na-ion vacancies, the system was assumed to remain electrically insulating and a uniform background charge was added in order to evaluate the electrostatic interactions. The minimum energy path for Na-ion migration was estimated using the "nudged elastic band" (NEB) method [35–37] as programed in the QUANTUM ESPRESSO package, using five images between each metastable configuration. For each minimum energy path, the migration energy, E_m, was determined as the energy difference between the lowest and highest energy of the path. For systems having appreciable concentrations of vacancies considered here, a reasonable approximation to the calculated activation energy could be determined from $E_a^{\mathrm{calc}} \approx E_m$ to be compared with the experimental activation energy determined from Eq. (1). Simulation cells for vacancy migration in Na_3SbS_4 were based on $2 \times 2 \times 2$ replicas of its bulk lattice, while for Na_3SbS_3 the simulation cells were $1 \times 2 \times 2$ replicas of its bulk lattice (in order to keep the calculations within a manageable range).

Simulations of surfaces and interfaces were performed using supercells in a slab geometry. The surface and interface energies were found to converge within five to seven layers of electrolyte. The surface energy of the electrolyte relative to vacuum could be calculated using slab simulations from the relationship

$$\gamma = \frac{E_{\mathrm{slab}} - N E_{\mathrm{bulk}}}{2A}. \tag{5}$$

Here E_{slab} denotes the total energy of the supercell containing N formula units of electrolyte and a vacuum region of at least 15 Å with a total slab area of $2A$. E_{bulk} denotes the total energy per formula unit of the bulk material. Simulations of idealized interfaces of Na_3SbS_4 with Na metal were carried out in supercells containing five to seven layers of electrolyte and four or more layers of Na. The simulation cells within the interface planes were fixed at the ideal electrolyte dimensions while all atom positions and the cell dimensions normal to the interfaces were optimized.

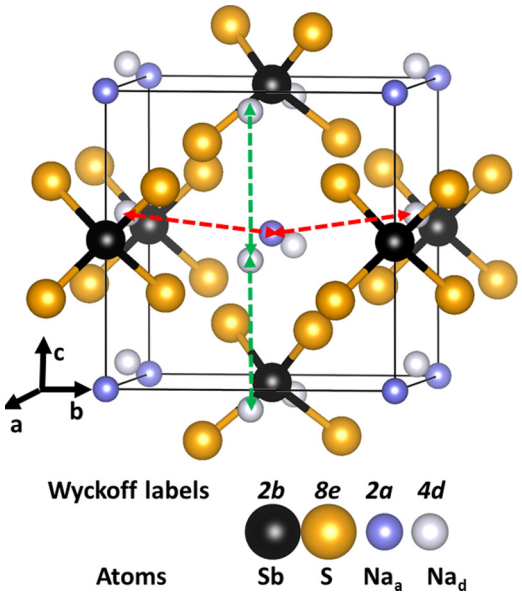

FIG. 1. Ball and stick model of Na_3SbS_4 in the tetragonal $P\bar{4}2_1c$ structure, using black and orange balls to indicate Sb and S sites, respectively. Inequivalent Na sites are indicated with blue and white balls. The red arrows illustrate possible vacancy migration paths between neighboring a and d sites, while the green arrows illustrate possible vacancy migration paths between neighboring d sites.

TABLE I. Lattice parameters and fractional coordinates for crystalline Na_3SbS_4 with space group $P\bar{4}2_1c$ (No. 114).

Lattice constant a (Å)	7.09[a]
	7.16[b]
	7.15[c]
	7.16[d]
Lattice constant c (Å)	7.25[a]
	7.29[b]
	7.28[c]
	7.29[d]
Fractional coordinate of Sb (2b)	(0, 0, $\frac{1}{2}$)[a,b,c,d]
Fractional coordinate of S (8e)	(0.29, 0.33, 0.19)[a]
	(0.29, 0.33, 0.18)[b]
	(0.30, 0.33, 0.18)[c]
	(0.29, 0.33, 0.19)[d]
Fractional coordinate of Na_a (2a)	(0, 0, 0)[a,b,c,d]
Fractional coordinate of Na_d (4d)	(0, $\frac{1}{2}$, 0.44)[a]
	(0, $\frac{1}{2}$, 0.44)[b]
	(0, $\frac{1}{2}$, 0.43)[c]
	(0, $\frac{1}{2}$, 0.44)[d]

[a]Simulation results; lattice constants scaled by 1.02.
[b]Experiment from Ref. [1].
[c]Experiment from Ref. [2], after shifting fractional coordinates by (0, 0, $\frac{1}{2}$).
[d]Experiment from Ref. [3].

III. RESULTS

A. Structures and energies

1. Structure of tetragonal Na_3SbS_4

The room-temperature phase of Na_3SbS_4 has been determined [1–3] to have a tetragonal structure with space group $P\bar{4}2_1c$ (No. 114) [38]. Figure 1 shows a ball and stick diagram of the structure. Table I lists the computed optimized lattice parameters and fractional atomic coordinates in comparison with measured results reported in recent literature. It is interesting to note that, although the three independent groups used different synthesis methods with different precursors and different furnace temperatures, the resulting product cooled to room temperature had essentially the same structure. The synthesis reported in Ref. [1] and in the present work used the precursor $Na_3SbS_4 \cdot 9H_2O$ (Schlippe's salt) with a processing temperature of 150 °C under vacuum. The synthesis reported in Ref. [2] used the precursors Na_2S, Sb_2S_3, and S and a processing temperature of 550 °C. The synthesis reported in Refs. [3,4] used elemental precursors of Na, Sb, and S and a processing temperature of 700 °C. The computed optimized latticed constants, scaled by the 1.02 factor to compensate for the LDA error, agree with the room-temperature experimental values within 0.07 Å and the fractional coordinates of the atomic positions agree within 0.01. There are two inequivalent Na-ion sites which we denote as Na_a and Na_d in accordance with their Wyckoff labels.

As a further comparison, Fig. 2 shows the x-ray data measured at room temperature for Na_3SbS_4 in the present work together with simulated spectra generated from MERCURY software [39] from the lattice parameters fit to neutron diffraction experiments reported in Ref. [1] and from the computed structure. Even though the neutron fitted results find a fractional occupancy (91%) for the Na_a site, the calculated structure with full occupancy shows negligible effects on the generated x-ray pattern at this wavelength, showing excellent agreement between the calculated and measured results.

2. Structure of cubic Na_3SbS_3

A related ionic conducting material is Na_3SbS_3 has been reported in the literature [13]. It has a cubic structure with the space group $P2_13$ (No. 198) [38], as shown in Fig. 3. Table II

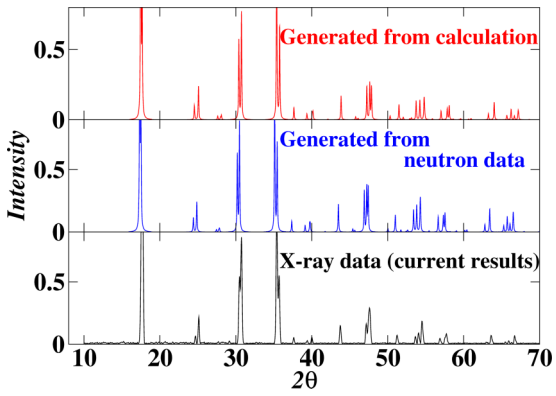

FIG. 2. Comparison of x-ray diffraction measurements and simulations for Na_3SbS_4 for the diffraction wavelength of $\lambda = 1.540\,56$ Å. The x-ray patterns were scaled to a maximum amplitude of 2 (arbitrary units) for the peak intensity at $2\theta = 17.4°$. The calculated results were generated from those reported in Table I. The neutron results were generated from the lattice parameters and fractional coordinates fit to neutron diffraction data, as reported in Ref. [1].

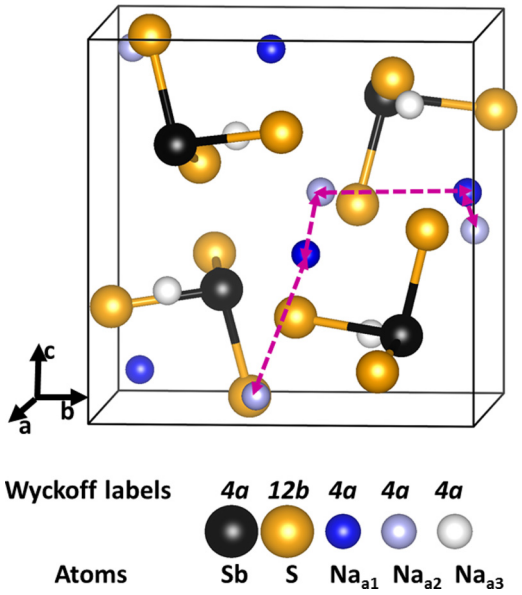

FIG. 3. Ball and stick model of Na_3SbS_3 in its $P2_13$ crystal structure, using black and orange balls to indicate Sb and S sites, respectively. Inequivalent Na sites are indicated with bright blue, pale blue, and white balls. The violet arrows illustrate possible vacancy migration paths between nearest-neighbor Na ions on alternating a_1 and a_2 sites.

lists the computed optimized lattice parameters (scaled by the 1.02 factor to compensate for the LDA error) and the fractional atomic coordinates, in comparison with measured results and again the agreement is quite good. Interestingly, Na_3SbS_3 is characterized by trigonal pyramidal SbS_3 units in contrast to the tetrahedral SbS_4 units of the Na_3SbS_4 structure.

3. *Energies and partial densities of states*

From differences in the total electronic energies of the computed optimized structures, it is possible to make a rough estimate of the reaction energies of Na_3SbS_4 itself and with metallic Na as "reactants" (R_i) into various decomposition

TABLE II. Lattice parameters and fractional coordinates for crystalline Na_3SbS_3 with space group $P2_13$ (No. 198).

Lattice constant a (Å)	8.57[a]
	8.64[b]
Fractional coordinate of Sb (4a)	(0.29, 0.29, 0.29)[a]
	(0.28, 0.28, 0.28)[b]
Fractional coordinate of S (12b)	(0.01, 0.25, 0.36)[a]
	(0.02, 0.25, 0.36)[b]
Fractional coordinate of Na$_{a3}$ (4a)	(0.82, 0.82, 0.82)[a]
	(0.83, 0.83, 0.83)[b]
Fractional coordinate of Na$_{a2}$ (4a)	(0.57, 0.57, 0.57)[a]
	(0.57, 0.57, 0.57)[b]
Fractional coordinate of Na$_{a1}$ (4a)	(0.06, 0.06, 0.06)[a]
	(0.06, 0.06, 0.06)[b]

[a]Simulation results; lattice constants scaled by 1.02.
[b]Experiment from Ref. [13].

TABLE III. Reaction energies estimated from calculated ground-state total energies according to Eq. (6).

Reaction	ΔE (eV)
$Na_3SbS_4 \rightarrow Na_3SbS_3 + S$	0.0
$Na_3SbS_4 + 2Na \rightarrow Na_3SbS_3 + Na_2S$	3.4
$Na_3SbS_4 + 8Na \rightarrow Na_3Sb + 4Na_2S$	9.0

"products" (P_j)

$$\sum_i R_i \rightarrow \sum_j P_j + \Delta E. \quad (6)$$

Here a positive value of ΔE corresponds to exothermic energy release. The reaction energies estimated in this way are expected to give qualitative information, since entropy and other finite-temperature effects are not taken into account. The results are summarized in Table III. For example, the results listed in Table III show that the total energies of Na_3SbS_4 and Na_3SbS_3 plus S in its ground state [40], have approximately the same energy. Another question of interest is how Na_3SbS_4 may react with metallic Na in its body-centered-cubic ground state. We find that the combination of one formula unit of Na_3SbS_4 and two formula units of Na can form Na_3SbS_3 and Na_2S with an exothermic energy release of 3.4 eV. Here we assume that Na_2S takes the cubic antifluorite structure [41]. Reacting one formula unit of Na_3SbS_4 with eight formula units of Na results in a further decomposition into four formula units of Na_2S plus one formula unit of Na_3Sb, which forms in a hexagonal structure [42], with an exothermic energy release of 9.0 eV. This apparent reactivity of the electrolyte/anode system has been seen in other sulfur-containing electrolytes [43]. It is our experience that similar systems may be stabilized either by the presence of kinetic barriers at the surface which prevent the reaction from occurring or by the formation of surface buffer layers which protect the system from decomposition.

The partial densities of states plots give qualitative information about the electronic structures as shown in Fig. 4, comparing $\langle N^a(E)\rangle$ curves for Na_3SbS_4 with those of Na_3SbS_3 and Na_2S. The partial densities of states curves of Na_3SbS_4 show that while nominally Sb has a formal charge of +5 in donating its valence electrons to S, a more realistic description involves covalent bonding between Sb and S. The contributions of Sb below the top of the valence band correspond to the bonding combinations of Sb and S states, while antibonding combinations comprise the conduction bands. Interestingly, the conduction bands of Na_3SbS_4 are split into two subbands, the lower band corresponding to antibonding states of S with the 5s states of Sb and the upper band corresponding to antibonding states of S with the 5p states of Sb. A similar pattern for the $\langle N^a(E)\rangle$ curves is found for the bonding and antibonding valence states associated with Sn and S in Li_4SnS_4 [44]. By contrast, for Na_3SbS_3, the formal charge of Sb is +3. This is reflected in the $\langle N^a(E)\rangle$ curves which show that both the bonding and antibonding states of S with the 5s states of Sb are within the valence band, and the conduction bands contain the antibonding states of S with the 5p states of Sb. For comparison, the partial densities of states curves for Na_2S are dominated by the filled 3p states of S.

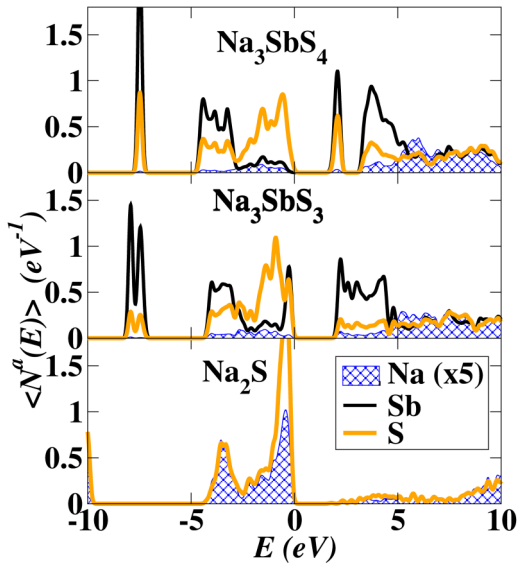

FIG. 4. Partial densities of states for the ground-state structures of Na_3SbS_4, Na_3SbS_3, and Na_2S. The zero of energy in these plots is taken as the top of the valence band of each material.

B. Mechanisms for Na-ion migration

1. *Na-ion migration in Na_3SbS_4*

The consensus in the literature [1–4,7–11] concerning Na-ion migration mechanisms in the Na_3SbS_4 family of materials is that Na-ion vacancies are important. For example, Ref. [1] reports a conductivity of 1 mS/cm at room temperature and their diffraction analysis indicates 9% Na-ion vacancies in their sample. Consistent with this previous work, our NEB simulations find that Na-ion vacancy diffusion along the **a** or **b** axis is very efficient with a migration barrier of $E_m = 0.06$ eV. Na-ion vacancy diffusion along the **c** axis is also efficient with a barrier of $E_m = 0.08$ eV. The corresponding energy path diagrams are given in Fig. 5, generated within the nudged elastic band approach for Na-ion vacancy migration near the crystallographic directions. For a sample with a native population of vacancies, this analysis implies that calculated

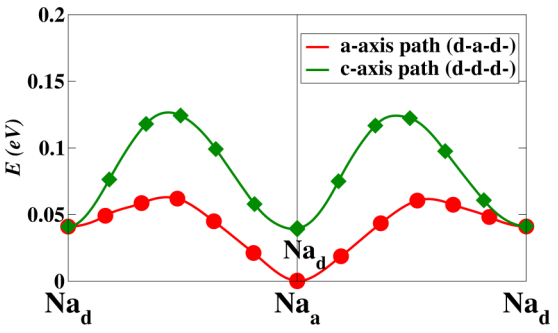

FIG. 5. Computed energy path diagram for Na-ion vacancy migrations in Na_3SbS_4 corresponding to the nearest-neighbor hops indicated in Fig. 1 for migration along the **a** or **b** axis (red symbols and line) and along the **c** axis (green symbols and line). The symbols represent directly calculated configurations, while the lines are smooth interpolations between NEB images. The zero of energy is set at the energy of a Na-ion vacancy at a Na_a site.

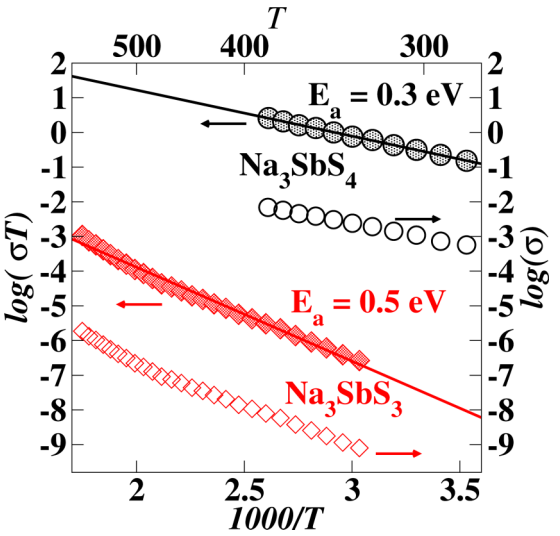

FIG. 6. Plot of experimentally measured values of $\log(\sigma T)$ (left, filled symbols and lines) and $\log\sigma$ (right, open symbols) versus $1000/T$ where σ is given in units of S/cm and T is given in units of Kelvin for Na_3SbS_4 (black symbols from present work) and Na_3SbS_3 (red symbols from Ref. [13]). Lines represent least-square fits to the $\log(\sigma T)$ data. The values of the activation energies $E_a^{\text{expt.}}$ as determined from the fits are indicated.

activation energy for this system should be $E_a^{\text{calc}} = E_m = 0.1$ eV. The experimental measurements of conductivity versus temperature for this system are shown in Fig. 6 where the experimental activation energy determined by fitting the conductivity data to Eq. (1) is found to be $E_a^{\text{expt.}} = 0.3$ eV [45]. The discrepancy between the calculated and experimental estimates of the activation energy, is outside the expected error of the NEB approximation of ± 0.1 eV. The model calculations are performed on ideal single crystals assumed to have a native population of Na-ion vacancies, while the experiments are performed with nano- and microsized particles cold-pressed to form pellets. The discrepancy could perhaps be attributed to the energetic contributions of Na-ion vacancy formation or the effects of grain boundaries resistance, for example.

2. *Na-ion migration in Na_3SbS_3*

We also considered vacancy migration within bulk Na_3SbS_3. In this material, the most stable vacancy site is found to be at the Na_{a3} site. Relative to the Na_{a3} vacancy configuration, vacancies at the Na_{a1} and Na_{a2} sites were found to have energies of 0.26 and 0.40 eV, respectively. We find that the most efficient vacancy migration for this material occurs between the Na_{a1} and Na_{a2} sites as defined in Fig. 3 and Table II. The corresponding energy path diagram is shown in Fig. 7. For the ideal lattice, it is possible to traverse the crystal hopping alternately between these two sites, with a net migration barrier of $E_m = 0.4$ eV. Hops involving vacancies at Na_{a3} sites were found to increase the migration barriers to approximately 1 eV. Therefore, for a sample of Na_3SbS_3 containing an appreciable population of Na-ion vacancies, the calculations predict the activation energy to be $E_a^{\text{calc}} = E_m = 0.4$ eV. The measured activation energy which is shown in Fig. 6, replotted from the experimental

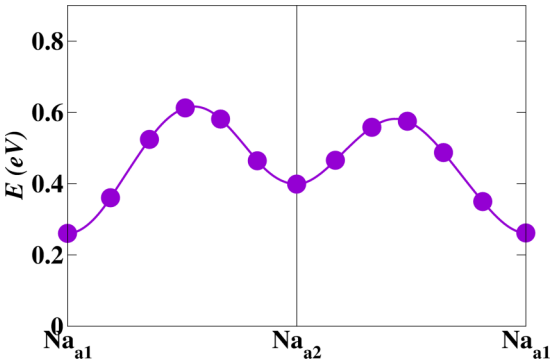

FIG. 7. Computed energy path diagram for Na-ion vacancy migrations in bulk Na_3SbS_3 corresponding to nearest-neighbor hops between Na_{a1} and Na_{a2} sites. The symbols represent directly calculated configurations, while the lines are smooth interpolations between NEB images. The zero of energy is set at the energy of a Na-ion vacancy at a Na_{a3} site.

results of Ref. [13] using the Nernst-Einstein form of Eq. (1), is $E_a^{\text{expt.}} = 0.5$ eV. As in the case of Na_3SbS_4, the calculated activation energy for the idealized system underestimates the experimental results. However, both the simulation and experimental results suggest that Na_3SbS_3 is a viable ionic conductor even though its conductivity value is significantly smaller and activation energy significantly higher than that of Na_3SbS_4.

C. Surfaces and interfaces

One of the important potential advantages of solid electrolytes in battery technology is their stability, especially with respect to electrode materials. For the present system, we investigated the properties of the interface of Na_3SbS_4 and Na metal within a $Na/Na_3SbS_4/Na$ symmetric cell. Figure 8 shows the voltage versus time plot for 40 cycles of the symmetric cell using a current density of 0.1 mA/cm^2 and a cycle time of 30 min for each positive or negative polarization. The room-temperature ionic conductivity in this symmetric cell was found to be 0.6 and 0.7 mS/cm for dc and ac measurements, respectively. The corresponding ac conductivity for tetragonal Na_3SbS_4 with Al/C blocking electrodes was found to be 0.8 mS/cm at 25 °C. This value is slightly less than the value of 1 mS/cm found for this material in an earlier preparation [1], showing some sensitivity of the ionic conductivity to sample preparation. Following the 40 cycles, the symmetric cell was prepared for SEM and EDS analysis. Additional symmetric cells were allowed to cycle for greater than 300 cycles under the same conditions, achieving similar low interfacial resistance between the metallic sodium anode and the Na_3SbS_4 solid electrolyte. Figure 9 shows a micrograph of the resulting interface and the corresponding elemental analysis of the system. From this figure, it is evident that a solid electrolyte interphase (SEI) region forms at the interface, appearing at this magnification with a granular morphology.

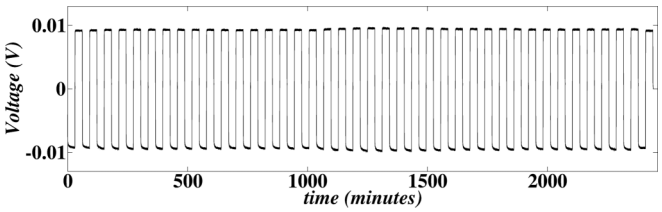

FIG. 8. Experimentally measured voltage versus time plot for a $Na/Na_3SbS_4/Na$ symmetric cell cycled 40 times with a current density of 0.1 mA/cm^2 and holding the positive and negative voltages for 30 min.

Atomic scale modeling can be used to first determine likely surface terminations of the electrolyte particles. Ideal surfaces for Na_3SbS_4 were investigated for surface normals in the (100), (001), and (110) directions, finding surface energies of $\gamma = 0.022$, 0.022, and 0.020 eV/Å^2, respectively, according to Eq. (5). The (110) surface energy depends slightly on the arrangement of the Na ion on the outer layer; however, these results suggest that all of these low index surfaces are approximately equally likely to form.

We also used computer modeling methods to study Na_3SbS_4/Na interfaces based on various electrolyte orientations and initial Na configurations. In all configurations considered, we found that metallic Na breaks Sb-S bonds, typically forming trigonal pyramidal SbS_3^{3-} and Na_2S groups at the interface. Figure 10 shows an example of a Na_3SbS_4/Na interface with the interface normal along the (001) axis of the electrolyte. The optimized configuration shown in Fig. 10(a) is metastable but very sensitive to variations in the Na positions. In this case, two of the outer layers of the electrolyte have tetrahedral SbS_4^{3-} ions converted into trigonal pyramidal SbS_3^{3-} ions, with excess Na_2S forming at the outer layer of the interface. The partial density of states analysis shows that the interior of the electrolyte in this case has the same distribution as the bulk, while the partial density of states corresponding to the interface layers reflect the altered electronic structure similar to that of crystalline Na_3SbS_3 as shown in Fig. 4. The Fermi level of the system is set by the metallic Na layers and lies within the band gap of the electrolyte, as is necessary for the electrolyte to perform its function of excluding electrons.

Another example of an interface model can be constructed with the interface normal oriented along the (110) direction of the Na_3SbS_4 lattice as shown in Fig. 11. In this case, only the outermost layers of the SbS_4^{3-} tetrahedra are converted to trigonal pyramidal SbS_3^{3-} groups. The partial densities of states plots again show that the interior of the electrolyte maintains its bulklike properties.

IV. DISCUSSION

In studying mechanisms for ionic conductivity, the nudged elastic band simulations of Na-ion vacancy migration in tetragonal Na_3SbS_4 finds the computed migration energy barriers to be $E_m = 0.1$ eV. This result suggests that for samples with an appreciable concentration of Na-ion vacancies, the tetrahedrally structured material should have a very similar ion conductivity mechanism to the higher temperature cubic material. Our results are similar to nudged elastic band results reported by Bo *et al.* [10] for cubic Na_3PSe_4. By contrast, our experimental results for the activation energy of Na-ion

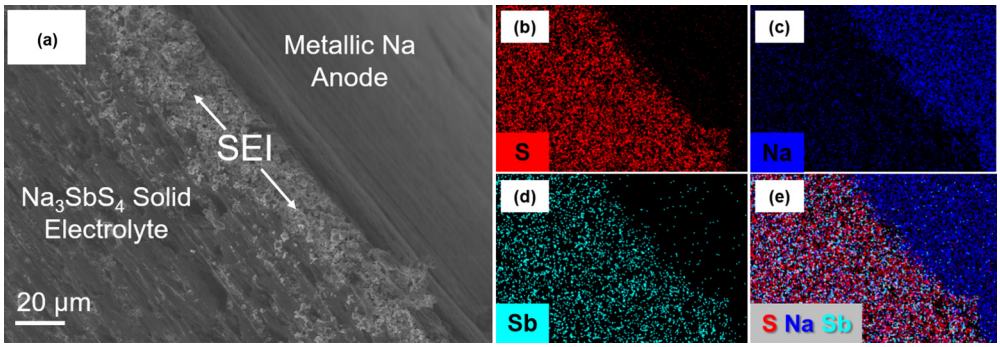

FIG. 9. (a) SEM image of the interface between a metallic sodium anode and the tetragonal Na_3SbS_4 solid electrolyte after 40 cycles in a $Na/Na_3SbS_4/Na$ symmetric cell configuration at a current density of 0.1 mA/cm^2 with the 20 μm scale indicated. Regions of pure electrolyte, pure anode, and the SEI are indicated. Panels (b), (c), (d), and (e) show the same interface sections of the SEM image as analyzed using the EDS to find elemental mappings of S, Na, Sb, and the three elements together, respectively.

conductivity in tetragonal Na_3SbS_4 of $E_a = 0.3$ eV, consistent with previous reports when analyzed using the Nernst-Einstein relation of Eq. (1) [1–4], are significantly larger. Further simulations are needed to better understand the detailed migration mechanisms such as the formation or stabilization of vacancies or perhaps the migration is dominated by intergrain transport.

Scanning electron microscopy of the Na_3SbS_4/Na interface (Fig. 9) shows that a significant solid electrolyte interphase region is formed after 40 cycles. Electrochemical analysis shows that this SEI region has appreciable ionic conductivity, perhaps related to the mechanisms modeled in this study. Interestingly, the model studies so far indicate that the interface reactions involve tetrahedral SbS_4 bonding complexes converting to trigonal pyramidal SbS_3 bonding complexes. However, in our interface model studies, we have not seen evidence of the further reduction to form Na_3Sb in analogy to the expected interface reaction in the Li_3PS_4/Li system for which it is expected that the following limiting reaction occurs [43,46,47]:

$$Li_3PS_4 + 8Li \rightarrow Li_3P + 4Li_2S. \quad (7)$$

Further challenges to understanding this interesting system remain including the question of whether it is possible to realize the low-energy barrier vacancy migration mechanism predicted by the model calculations, and the question of how Na_3SbS_4 is able to stabilize an appreciable concentration of vacancies. The latter question has been explored for related materials [10,11], but further study is warranted.

The nudged elastic band simulations of Na-ion vacancy migration in cubic Na_3SbS_3 finds the computed migration energy barriers to be $E_m = 0.4$ eV, a value which is within the expected model error of ± 0.1 eV of the experimental result of $E_a = 0.5$ eV reported in the literature [13]. In this mechanism, two-thirds of the Na ions (sites Na_{a1} and Na_{a2}) participate

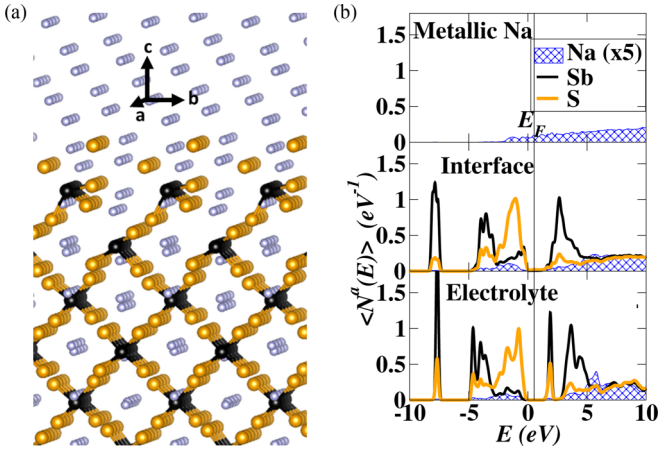

FIG. 10. (a) Ball and stick model of the simulated relaxed structure of a Na_3SbS_4 surface oriented along the (001) direction and interfaced with Na metal. The ball conventions for Sb and S is the same as in Fig. 1 and light blue balls represent both ionic and metallic Na. The indicated axes reference the Na_3SbS_4 lattice. (b) Corresponding partial densities of states analysis of this system, separately indicating the interior of the electrolyte, the interface region, and the metallic region in the bottom, middle, and top panels, respectively.

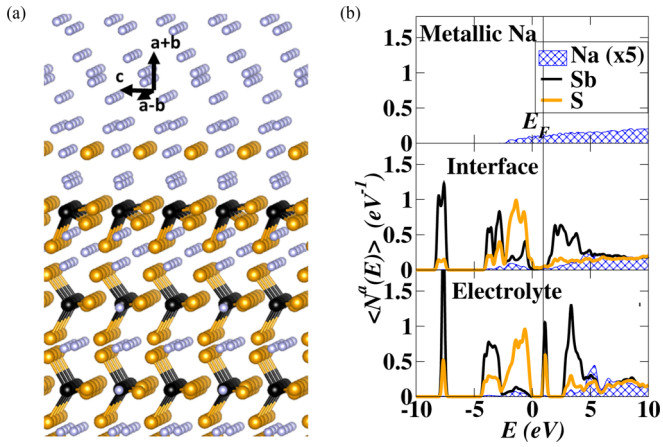

FIG. 11. (a) Ball and stick model of the simulated relaxed structure of a Na_3SbS_4 surface oriented along the (110) direction and interfaced with Na metal. The ball conventions for Sb and S are the same as in Fig. 1 and light blue balls represent both ionic and metallic Na. The indicated axes reference the Na_3SbS_4 lattice. (b) Corresponding partial densities of states analysis of this system, separately indicating the interior of the electrolyte, the interface region, and the metallic region in the bottom, middle, and top panels, respectively.

in the ionic conductivity, while site Na_{a3} is expected to not participate due to its larger hop distance and correspondingly larger activation barrier. While Na_3SbS_3 itself is not expected to be an efficient solid electrolyte material, our models of Na_3SbS_4/Na interfaces indicate that Na_3SbS_3 groups readily form as a decomposition product. While this interface Na_3SbS_3 is unlikely to be arranged in the same cubic structure as the bulk material particularly since excess Na_2S is also involved, we expect that its ion conducting properties may be related, helping to explain the experimental Na_3SbS_4/Na interface.

V. SUMMARY AND CONCLUSIONS

In this work, we have experimentally and computationally investigated the electrolyte properties of bulk tetragonal Na_3SbS_4 and its interface with metallic sodium. Experimentally the bulk material is found to have an ionic conductivity of greater than 0.8 mS/cm at room temperature (294.26 K). When the samples are cycled in a symmetric Na/Na_3SbS_4/Na cell at room temperature with a current density of 0.1 mA/cm^2 for 40 cycles, an SEI layer was found to form at the interface. This SEI layer was found to be ionically conductive at room temperature, allowing for bulk Na_3SbS_4 to cycle efficiently with a metallic sodium anode, reducing the conductivity by approximately 0.1 mS/cm, as evidenced by the difference between the ac and dc conductivity measurements.

Nudged elastic band simulations of Na-ion vacancy migration in tetragonal Na_3SbS_4 finds vacancy migration to be very efficient, with a small barrier of $E_m = 0.1$ eV, consistent with literature results on related materials. Further work is needed for reconciliation with experiment.

Simulations of models of the Na_3SbS_4/Na interface suggest the formation of Na_3SbS_3-like groups at the interface which contribute to both the relative stability of the interface and to its good ionic conductivity.

ACKNOWLEDGMENTS

The computational portion of this work was supported by NSF Grant No. DMR-1507942. Computations were performed on the Wake Forest University DEAC cluster, a centrally managed resource with support provided in part by the University. The experimental portion of the work was sponsored by the U.S. Department of Energy (DOE), Office of Science, Basic Energy Sciences, Materials Sciences and Engineering Division, and the synthesis and characterization was completed at the Center for Nanophase Materials Sciences, which is a DOE Office of Science User Facility. Z.D.H. gratefully acknowledges support from the National Science Foundation Graduate Research Fellowship under Grant No. DGE-1650044 and the Georgia Tech-ORNL Fellowship. Helpful discussions with Hui Wang from the University of Louisville and Yan Chen from Oak Ridge National Laboratory are gratefully acknowledged.

[1] H. Wang, Y. Chen, Z. D. Hood, G. Sahu, A. S. Pandian, J. K. Keum, K. An, and C. Liang, Angew. Chem., Int. Ed. **55**, 8551 (2016).
[2] A. Banerjee, K. H. Park, J. W. Heo, Y. J. Nam, C. K. Moon, S. M. Oh, S.-T. Hong, and Y. S. Jung, Angew. Chem., Int. Ed. **55**, 9634 (2016).
[3] L. Zhang, D. Zhang, K. Yang, X. Yan, L. Wang, J. Mi, B. Xu, and Y. Li, Adv. Sci. **3**, 1600089 (2016).
[4] D. Zhang, X. Cao, D. Xu, C. Yu, W. Hu, X. Yan, J. Mi, B. Wen, L. Wang, and L. Zhang, arXiv:1707.05166.
[5] A. Hayashi, K. Noi, A. Sakuda, and M. Tatsumisago, Nat. Commun. **3**, 856 (2012).
[6] M. Jansen and U. Henseler, J. Solid State Chem. **99**, 110 (1992).
[7] L. Zhang, K. Yang, J. Mi, L. Lu, L. Zhao, L. Wang, Y. Li, and H. Zeng, Adv. Energy Mater. **5**, 1501294 (2015).
[8] Z. Zhu, I.-H. Chu, Z. Deng, and S. P. Ong, Chem. Mater. **27**, 8318 (2015).
[9] S.-H. Bo, Y. Wang, and G. Ceder, J. Mater. Chem. A **4**, 9044 (2016).
[10] S.-H. Bo, Y. Wang, J. C. Kim, W. D. Richards, and G. Ceder, Chem. Mater. **28**, 252 (2016).
[11] N. J. J. de Klerk and M. Wagemaker, Chem. Mater. **28**, 3122 (2016).
[12] Y. Wang, W. D. Richards, S. P. Ong, L. J. Miara, J. C. Kim, Y. Mo, and G. Ceder, Nat. Mater. **14**, 1026 (2015).
[13] C. Pompe and A. Pfitzner, Z. Anorg. Allg. Chem. **639**, 296 (2013).
[14] J. Y. Howe, L. A. Boatner, J. A. Kolopus, L. R. Walker, C. Liang, N. J. Dudney, and C. R. Schaich, J. Mater. Sci. **47**, 1572 (2012).
[15] J. Maier, *Physical Chemistry of Ionic Materials* (Wiley, New York, 2004).
[16] R. A. Huggins, *Advanced Batteries* (Springer, New York, 2009).
[17] C. R. A. Catlow, Annu. Rev. Mater. Sci. **16**, 517 (1986).
[18] P. Hohenberg and W. Kohn, Phys. Rev. **136**, B864 (1964).
[19] W. Kohn and L. J. Sham, Phys. Rev. **140**, A1133 (1965).
[20] P. E. Blöchl, Phys. Rev. B **50**, 17953 (1994).
[21] N. A. W. Holzwarth, A. R. Tackett, and G. E. Matthews, Comput. Phys. Commun. **135**, 329 (2001), available from the website http://pwpaw.wfu.edu.
[22] P. Giannozzi, S. Baroni, N. Bonini, M. Calandra, R. Car, C. Cavazzoni, D. Ceresoli, G. L. Chiarotti, M. Cococcioni, I. Dabo, A. D. Corso, S. de Gironcoli, S. Fabris, G. Fratesi, R. Gebauer, U. Gerstmann, C. Gougoussis, A. Kokalj, M. Lazzeri, L. Martin-Samos, N. Marzari, F. Mauri, R. Mazzarello, S. Paolini, A. Pasquarello, L. Paulatto, C. Sbraccia, S. Scandolo, G. Sclauzero, A. P. Seitsonen, A. Smogunov, P. Umari, and R. M. Wentzcovitch, J. Phys.: Condens. Matter **21**, 395502 (2009), available from the website http://www.quantum-espresso.org.
[23] A. Kokalj, J. Mol. Graphics Modell. **17**, 176 (1999), code available at the website http://www.xcrysden.org.
[24] A. Kokalj, Comput. Mater. Sci. **28**, 155 (2003).

[25] K. Momma and F. Izumi, Appl. Crystallogr. **44**, 1272 (2011), code available from the website http://jp-minerals.org/vesta/en/.
[26] J. P. Perdew and Y. Wang, Phys. Rev. B **45**, 13244 (1992).
[27] Y. A. Du and N. A. W. Holzwarth, Phys. Rev. B **76**, 174302 (2007).
[28] N. A. W. Holzwarth, N. D. Lepley, and Y. A. Du, J. Power Sources **196**, 6870 (2011).
[29] Y. A. Du and N. A. W. Holzwarth, Phys. Rev. B **81**, 184106 (2010).
[30] N. D. Lepley and N. A. W. Holzwarth, J. Electrochem. Soc. **159**, A538 (2012).
[31] N. D. Lepley, N. A. W. Holzwarth, and Y. A. Du, Phys. Rev. B **88**, 104103 (2013).
[32] K. Senevirathne, C. S. Day, M. D. Gross, A. Lachgar, and N. A. W. Holzwarth, Solid State Ionics **233**, 95 (2013).
[33] Z. D. Hood, C. Kates, M. Kirkham, S. Adhikari, C. Liang, and N. A. W. Holzwarth, Solid State Ionics **284**, 61 (2015).
[34] N. A. W. Holzwarth, G. E. Matthews, R. B. Dunning, A. R. Tackett, and Y. Zeng, Phys. Rev. B **55**, 2005 (1997).
[35] H. Jónsson, G. Mills, and K. W. Jacobsen, in *Classical and Quantum Dynamics in Condensed Phase Simulations*, edited by B. J. Berne, G. Ciccotti, and D. F. Coker (World Scientific, Singapore, 1998), pp. 385–404.
[36] G. Henkelman, B. P. Uberuaga, and H. Jónsson, J. Chem. Phys. **113**, 9901 (2000).
[37] G. Henkelman and H. Jónsson, J. Chem. Phys. **113**, 9978 (2000).
[38] *International Tables for Crystallography, Volume A: Space-Group Symmetry*, 5th rev. ed., edited by T. Hahn (Kluwer, Dordrecht, 2002). The symmetry labels used in this work are all based on this reference.
[39] Mercury 3.5.1, 2014; developed and distributed by the Cambridge Crystallographic Data Centre, http://www.ccdc.cam.ac.uk/mercury/.
[40] S. J. Rettig and J. Trotter, Acta Crystallogr., Sect. C: Struct. Chem. **43**, 2260 (1987).
[41] W. Buhrer and H. Bill, J. Phys. C **13**, 5495 (1980).
[42] G. Brauer and E. Zintl, Z. Phys. Chem. **37B**, 325 (1937).
[43] N. D. Lepley and N. A. W. Holzwarth, Phys. Rev. B **92**, 214201 (2015).
[44] A. Al-Qawasmeh, J. Howard, and N. A. W. Holzwarth, J. Electrochem. Soc. **164**, A6386 (2017).
[45] Note that temperature-dependent conductivity data fit to a simple exponential form $\sigma = \sigma_0 \exp(-E'_a/kT)$, gives a smaller activation energy of $E'_a = 0.2$ eV.
[46] Y. Zhu, X. He, and Y. Mo, ACS Appl. Mater. Interfaces **7**, 23685 (2015).
[47] Y. Zhu, X. He, and Y. Mo, Adv. Sci. **4**, 1600517 (2017).